Electrokinetic, electrochemical, and electrostatic surface potentials of the pristine water liquid–vapor interface

View Online   Export Citation   CrossMark

Maximilian R. Becker,[1] [ID] Philip Loche,[1,2] [ID] and Roland R. Netz[1,a)] [ID]

AFFILIATIONS

[1] Fachbereich Physik, Freie Universität Berlin, 14195 Berlin, Germany
[2] Laboratory of Computational Science and Modeling, IMX, Ecole Polytechnique Federale de Lausanne, 1015 Lausanne, Switzerland

[a)]Author to whom correspondence should be addressed: rnetz@physik.fu-berlin.de

ABSTRACT

Although conceptually simple, the air–water interface displays rich behavior and is subject to intense experimental and theoretical investigations. Different definitions of the electrostatic surface potential as well as different calculation methods, each relevant for distinct experimental scenarios, lead to widely varying potential magnitudes and sometimes even different signs. Based on quantum-chemical density-functional-theory molecular dynamics (DFT-MD) simulations, different surface potentials are evaluated and compared to force-field (FF) MD simulations. As well explained in the literature, the laterally averaged electrostatic surface potential, accessible to electron holography, is dominated by the trace of the water molecular quadrupole moment, and using DFT-MD amounts to +4.35 V inside the water phase, very different from results obtained with FF water models which yield negative values of the order of −0.4 to −0.6 V. Thus, when predicting potentials within water molecules, as relevant for photoelectron spectroscopy and non-linear interface-specific spectroscopy, DFT simulations should be used. The electrochemical surface potential, relevant for ion transfer reactions and ion surface adsorption, is much smaller, less than 200 mV in magnitude, and depends specifically on the ion radius. Charge transfer between interfacial water molecules leads to a sizable surface potential as well. However, when probing electrokinetics by explicitly applying a lateral electric field in DFT-MD simulations, the electrokinetic ζ-potential turns out to be negligible, in agreement with predictions using continuous hydrodynamic models. Thus, interfacial polarization charges from intermolecular charge transfer do not lead to significant electrokinetic mobility at the pristine vapor–liquid water interface, even assuming these transfer charges are mobile in an external electric field.

I. INTRODUCTION

At charged surfaces that are in contact with an aqueous salt solution, an ionic double layer forms[1] which creates an electrostatic potential difference between the surface and the solution, often called, rather indiscriminatorily, the surface potential. Even at the nominally uncharged air–water interface, different ions exhibit different interfacial affinities, which gives for most ion combinations rise to a pronounced ionic charge separation normal to the interface and thus to a non-vanishing surface potential.[2,3] Since even pure water contains ions due to autoprotolysis, this mechanism is also operative in the absence of added salt.[4]

However, a surface potential is also present in the absence of any ions due to the molecular water dipole in conjunction with an anisotropic water orientation at the interface and due to the quadrupolar charge distribution within a water molecule. Consequently, both the dipole and the quadrupole moment of water contribute to the surface potential.[5–8] The laterally averaged surface potential of liquid water (when not mentioned otherwise in this paper, defined as the electrostatic potential inside the liquid water

phase compared to the vapor phase) from density-functional-theory molecular-dynamics (DFT-MD) simulations was determined to be +3.1, +3.6, and +4.3 V, depending on the simulation setup,[7,9,10] in rather good agreement with electron holography measurements of vitrified ice.[11,12] Employing a similar experimental technique, the surface potential of liquid water has recently been experimentally determined to be +4.48 V.[13] In contrast, simple three-point-charge force-field molecular-dynamics (FF-MD) simulations yield a negative surface potential in the range of −0.4 to −0.6 V; yet, the interfacial water structure is rather similar for DFT-MD and FF-MD simulations of the air–water interface.[4] These at-first-sight puzzling results are due to the trace of the water quadrupolar tensor, which is very different for DFT and FF water models and dominates the surface potential but does not influence the water–water interactions and thus is rather irrelevant for the interfacial water structure.[6–8,10,14,15]

In fact, there are many different ways of experimentally measuring the surface potential of aqueous interfaces, which all give rise to significantly different values; hence, different experimental measurements define different surface potentials.

In electrochemical experiments, electrostatic potential differences acting on finite-size ions are reported. They fundamentally differ from the above-mentioned electron holography experiments since the ions do not probe the interior electrostatic potentials of water molecules. Therefore, the electrochemical potential does not reflect the electrostatic potential across an interface that is laterally averaged including the interior of the water molecules.[10,16,17] Moreover, water molecules are anisotropically oriented around ions, which gives rise to an additional electrostatic contribution to the electrochemical potential. Thus, in the hypothetical situation where an ion crosses the air–water interface, the electrostatic work done on the ion charge is roughly given by the sum of the air–water surface potential and the potential across the ion hydration shell.[16,18,19] By this, the quadrupolar water contribution to the electrochemical potential cancels almost entirely out, which explains why DFT and FF simulations give quite comparable results for electrochemical potential across the air–water interface.[10,16,17] In other words, the sum of the dipolar contributions from the air–water interface and the water–ion interface results in the electrochemical potential, which is considerably smaller than the laterally averaged surface potential (including water interiors) but still nonzero. However, the situation is slightly complicated by the fact that ions are surrounded by a partial hydration shell even in the vapor phase,[20,21] which means that the hypothetical experiment of an ion crossing the vapor–water interface is, in fact, a rather complicated scenario. Interestingly, it was recently suggested that the electrochemical potential plays a crucial role in explaining like-charge attraction between surfaces and particles in monovalent salt solutions;[22,23] this constitutes a mechanism that is fundamentally different from the like-charge attraction between highly charged surfaces in multivalent salt solutions, which is caused by correlation effects that are not captured by mean-field theory.[24–26]

Surface potentials have also been determined from the kinetic energy loss of high-energy electrons[27] or helium nuclei[28] that cross the air–water interface. Depending on their kinetic energy, the particles do also probe the electrostatics inside the water molecules and thus perform some type of lateral average over the electrostatic surface potential. However, it should be noted that the ionizing

radiation has to cross two interfaces, namely, the air–water interface and the water–substrate interface to the radioactive source or the detector, depending on the experimental setup. It transpires that what is measured in these experiments is not the absolute surface potential of the air–water interface but rather the surface potential difference between the air–water interface and the second water–solid interface, which depends crucially on the solid type. The same statement holds also true for surface-potential measurements via the vibrating plate method[29] since, in these measurements, a counter electrode has to be inserted into the liquid bulk material. Thus, in order to correctly infer the water–vapor surface potential from such experimental measurements, one would need to subtract the solid–water potential, which, in general, is not available and complicated by itself.

In x-ray photoelectron spectroscopy,[30,31] sum-frequency generation (SFG), and second-harmonic generation (SHG),[29,32–34] the situation is again different: here, an effective electrostatic potential is probed at positions inside the water molecules; in the case of vibrational spectroscopy, the potential reflects some type of average over the positions of the electrons and nuclei that are involved in the vibrational band, in the case of photoelectron spectroscopy, the potential reflects an electrostatic contribution to the work done by the electron as it leaves the water molecule. Since the electrostatic potential inside the water molecules is not well described by force-field water models, as explained above, this necessitates the use of DFT-MD simulations in order to predict surface potential contributions to x-ray photoelectron and non-linear optical spectra.

Experimentally straightforward is the measurement of the electrokinetic mobility of a particle or a surface in an externally applied electric field. By using a number of approximations and assumptions, this mobility is typically converted into the electrostatic potential difference between the bulk liquid phase and the shear plane at which the liquid is assumed to fulfill a no-slip boundary condition, which defines the so-called ζ-potential. It has been experimentally known for a long time that the vapor–water interface exhibits a negative ζ-potential compared to the water bulk,[35–38] which, in early works, was interpreted in terms of enhanced interfacial adsorption of hydroxide ions with respect to hydronium ions. However, this interpretation contradicts the experimental fact that the surface tension of acids decreases and that of bases increases with concentration, which indicates that hydronium has a slight propensity to bind to the vapor–solution interface, while hydroxide is slightly repelled from the vapor–solution interface,[4,39,40] as confirmed by sum frequency generation and second-harmonic generation experiments[41] as well as simulations.[4,42] Although the carbonate ion has a slight affinity to the air–water interface,[43] its interface affinity is not strong enough to cause the magnitude of the experimentally measured negative ζ-potentials.[44] Alternative explanations for the negative ζ-potential of neat water interfaces invoke the adsorption of negatively charged surface-active impurities, which are omnipresent even in pure lab water,[40,44–46] although it should be noted that this interpretation is controversially discussed.[47] It has also been suggested that the water dipolar orientation at the water–vapor surface, which gives rise to an electrostatic surface potential, as has been discussed above, translates into electrokinetic mobility.[48,49] However, in later simulation and analytic work, it was shown that the interfacial orientation of overall neutral water

molecules cannot lead to stationary electrokinetic flow in DC electric fields.[50–52]

According to yet another interpretation, the ζ-potential of the pristine air–water interface is produced by intermolecular charge transfer due to a difference in the spatial distribution of hydrogen-bond donating and accepting water molecules close to the vapor–water interface, which causes an inhomogeneous transfer-charge distribution.[53–56] This prompts the question of whether charge transfer between the water molecules at the air–water interface can principally give rise to electrophoretic motion in an externally applied electric field. Our explicit DFT simulations in the presence of an electric field that is tangential to the interface indicate that the transferred charges cannot move in an applied field, and even if they could, hydrodynamic theory predicts the ζ-potential to be much smaller than what is measured experimentally. Clearly, more work along these lines is required in order to rule out charge transfer as a cause of electrophoresis at the air–water interface and also to understand the consequences of interfacial charge transfer in general.

In essence, at least four different definitions of the surface potential of liquid water interfaces exist, related to electrokinetic, electrochemical, electron-holography, and nonlinear spectroscopy or photoelectron experiments. The relation between these different surface potentials is not always clearly discussed in the literature, the confusion is enhanced by the fact that different simulation and analytic models give vastly different results even when identical definitions of a surface potential are used. In this paper, we attempt

to clarify some of these issues by comparing DFT-MD and FF-MD results for different surface potential definitions and by discussing the microscopic mechanisms that determine their different properties. As a result, we arrive at a unified description of the electrostatic and electrokinetic properties of the air–water interface in terms of electrokinetic, electrochemical, and electrostatic surface potentials.

II. RESULTS

A. Simulation model

To study surface potentials at the neat vapor–water interface, we conduct DFT-MD simulations of the system shown in Fig. 1(a), which contains 352 water molecules in a simulation box of $2 \times 2 \times 6$ nm^3 that form a stable vapor–liquid water slab geometry as demonstrated by the atom mass density profile $\rho_{atom}(z)$ in Fig. 1(b). The DFT-MD atomistic mass density profile (red line) displays oscillations on a short spatial scale that reflect water layering and is due to the short sampling time, as demonstrated by comparison with FF-MD simulations with the extended simple point charge (SPC/E) model[76] of the same system size but over much longer times (black line). In Sec. S1 of the supplementary material, we present an in-depth discussion of the DFT-MD and FF-MD sampling characteristics and show that similar density oscillations also appear in FF-MD simulation when conducted for short simulation times. Profiles at the air–water interface, such as mass or charge profiles, that are determined in the lab frame are broadened by capillary waves and thus subject to finite-size effects. Therefore, in order
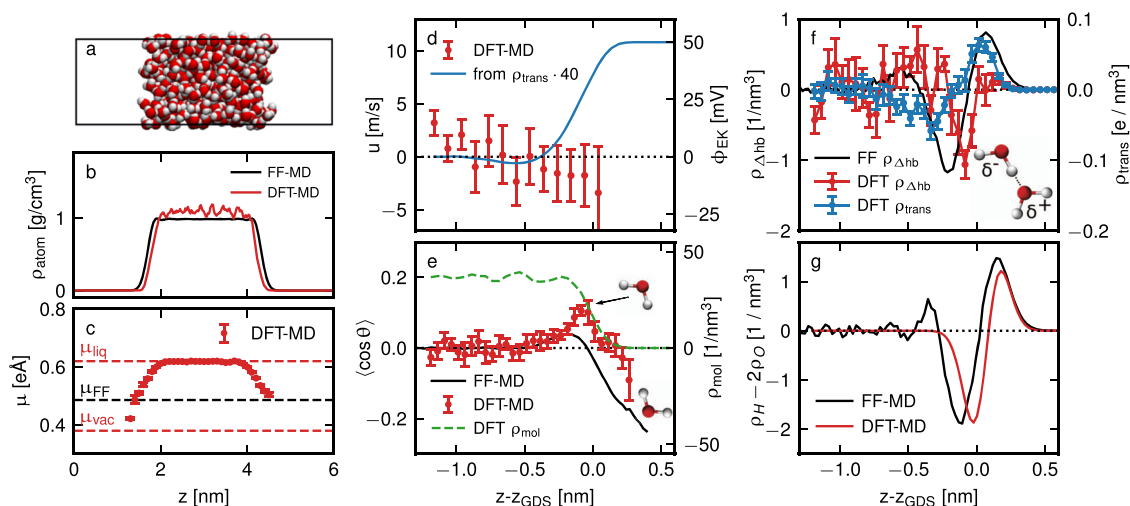

FIG. 1. (a) DFT-MD simulation snapshot of 352 water molecules that form a liquid slab in a box of $2 \times 2 \times 6$ nm^3. (b) Atomic mass density profile $\rho_{atom}(z)$ from 100 ps DFT-MD (red) and 20 ns FF-MD (black) simulations, both with 352 water molecules. (c) Water molecular dipole moment profile from DFT-MD (red circles). The bulk value $\mu = 0.62$ eÅ and the vacuum value $\mu = 0.38$ eÅ (horizontal red broken lines) compare well to the experimental values of 0.60 ± 0.125 eÅ for liquid water[66] and 0.386 eÅ for vacuum.[67] The black broken line shows the dipole moment of the SPC/E FF model. (d) Water velocity profile from DFT-MD for an applied tangential field of $E_\parallel = 257$ mV/nm (red points, left scale), the right scale shows the electrokinetic potential according to Eq. (3). The predicted flow profile from the DFT-MD transfer-charge profile $\rho_{trans}(z)$ according to Eq. (1) is multiplied by a factor of 40 (blue line). (e) Water orientational profile binned with respect to molecular COM positions, where θ is the angle between the interface normal and the water dipoles, from DFT-MD (red circles) and FF-MD (black line). The green broken line is the molecular center-of-mass water density profile $\rho_{mol}(z)$ from DFT (right scale). (f) Hydrogen bond difference $\rho_{\Delta hb}(z)$ between accepted and donated hydrogen bonds, binned with respect to the water molecular center of mass from DFT-MD (red circles) and FF-MD (black line). The blue circles show the molecular transfer-charge density $\rho_{trans}(z)$ from a DDEC6 atomic charge analysis of the DFT-MD data. (g) Hydrogen/oxygen density difference $\rho_H(z) - 2\rho_O(z)$ from DFT-MD (fitted, red line) and FF-MD (black line), binned with respect to atom positions.

to meaningfully compare FF-MD and DFT-MD simulation results, we always use identical system sizes. In Sec. S2 of the supplementary material, we discuss in detail finite-size effects and demonstrate that electrostatic potential profiles are not subject to significant finite-size effects. Further simulation details are presented in Sec. IV.

B. Electrokinetic surface potential ϕ_{EK}

If charge transfer between water molecules at the interface generated mobile charges that can move in response to an external electric field, a tangential electric field could perform work on these charges and produce a net shear flow at the interface, corresponding to a finite ζ-potential. To study this scenario of charge-transfer-induced electrokinetic mobility, we apply an electric field of $E_\parallel = 257$ mV/nm parallel to the vapor–water interface in the DFT simulations and record the induced water motion. The same simulation procedure has been previously used to calculate ζ-potentials at surfactant monolayers and lipid bilayers using FF-MD.[45,57] The treatment of finite electric fields as implemented in the software package CP2K accounts for the Berry phase[58] and has been successfully applied to the auto-dissociation of liquid water[59] and Raman spectroscopy.[60] We obtain the mean water velocity profile $u(z)$, based on the molecular center-of-mass (COM) velocities and binned according to the COM positions, depicted in Fig. 1(d) (red circles, left scale), which is zero within the sampling error. We now review the theoretical basis to convert the water flow profile $u(z)$ to experimentally reported ζ-potentials.

For a mobile charge density profile $\rho_{mob}(z)$ in the water phase and the presence of a tangential electric field $E_\parallel$, the hydrodynamic flow at the interface is governed by the Stokes equation,[61]

$$\frac{d}{dz}\left[\eta_\perp(z)\frac{d}{dz}u(z)\right] = -E_\parallel \rho_{mob}(z),$$ (1)

where $\eta_\perp(z)$ is the water viscosity profile, and $u(z)$ is the liquid velocity profile. A mobile charge by definition injects linear momentum into the fluid in an external electric field. Whether a charge distribution is mobile or not is not straightforward to say. In standard electrokinetic theory, the mobile charge distribution is due to an ionic double layer, and there is no question that an ion in the double layer can move and thus is mobile. For non-polarizable molecules and in the absence of charge transfer, it has been rigorously shown that for DC electric fields, only the molecular monopole density leads to electrokinetic flow.[50–52] If charge transfer between molecules is allowed for, DFT-MD simulations have to be used in order to find out whether a transfer-charge profile is mobile in an applied electric field and thus can be used within the context of Eq. (1). Using the definition of the perpendicular displacement field $dD_\perp(z)/dz = \rho_{mob}(z)$ due to the mobile charge distribution, the local approximate relation between displacement and electric field[61] $\varepsilon_0\varepsilon_\perp(z)E_\perp(z) = D_\perp(z)$, which defines the dielectric profile $\varepsilon_\perp(z)$, and the definition of the electrostatic potential $d\phi(z)/dz = -E_\perp(z)$, Eq. (1) is integrated twice to obtain the electrokinetic potential distribution,

$$\phi_{EK}(z) = \int_{z_l}^{z} \frac{\eta_\perp(z')}{E_\parallel \varepsilon_0 \varepsilon_\perp(z')} \frac{du(z')}{dz'} dz',$$ (2)

where we assumed that in the liquid bulk at z_l, the viscous stress vanishes, $du(z)/dz|_{z=z_l} = 0$, and the potential takes the value $\phi_{EK}(z_l) = 0$.

In the usual analysis of experimental electrokinetic data, the dielectric and viscosity profiles of water are assumed to be constant and set equal to their bulk values $\varepsilon_\perp(z) = \varepsilon_{bulk}$ and $\eta_\perp(z) = \eta_{bulk}$, which leads to the standard expression for the electrokinetic potential,

$$\phi_{EK}(z) = \frac{\eta_{bulk}}{\varepsilon_0 \varepsilon_{bulk} E_\parallel}[u(z) - u(z_l)].$$ (3)

Using the experimental values for the bulk dielectric constant $\varepsilon_{bulk} = 80$[62] and shear viscosity $\eta_{bulk} = 0.85$ mPa s[63] of water, we obtain the potential scale on the right side of Fig. 1(d). The shear viscosity of BLYP water was recently analyzed in the high-frequency regime and found to be similar to the TIP4P/2005 water force-field model,[64] which is known to reproduce experimental values quite well.[65] Therefore, the DFT-MD simulations presumably reproduce the viscous properties of water quite well. We define the bulk water velocity $u(z_l)$ as the mean water velocity in the range $z - z_{GDS} < -0.63$ nm.

On solid surfaces, in the usual scenario, the ζ-potential is defined as the potential at the shear surface, where the velocities of the solid and the water phase are identical. At the vapor–liquid interface, a more tricky scenario, the ζ-potential follows from the velocity of the vapor phase relative to the bulk liquid, which involves a subtle extrapolation since the water density, and thus the local viscosity, drops to almost zero in the vapor phase.[54] If we consider the mean of the two data points around the Gibbs dividing surface (GDS) in Fig. 1(d), where the water density is between the liquid and vapor values, the ζ-potential is estimated to be at most of the order of -12 mV and therefore substantially smaller compared to the experimental values in the order of -50 mV.[35–37] The high numerical cost of the DFT-MD simulation prevents us from performing substantially longer simulations with reduced numerical errors.

To scrutinize the connection between possible electrokinetic water mobility and charge transfer, which was intensely discussed in the literature,[53–56] we calculate DDEC6 atomic transfer charges every 50 fs of our DFT-simulations.[68] By adding up the atomic transfer charges for each water molecule, we obtain the molecular transfer-charge density profile $\rho_{trans}(z)$ in Fig. 1(f) (blue spheres, right scale), which is calculated from an equilibrium trajectory in the absence of an externally applied electrical field. In Sec. S3 of the supplementary material, we show that $\rho_{trans}(z)$ and the bulk dielectric constant of water do not change significantly if an electric field of 257 mV/nm is applied. Thus, the applied electric field in our simulations, which is quite high in order to minimize the numerical error, does not change the equilibrium transfer-charge profile. Indeed, charge transfer gives rise to a local enrichment of positively charged water molecules at the vapor–water interface, accompanied by a broad negatively charged region toward the water phase and a slight positive hump further away from the interface; this triple charge layer is in qualitative agreement with the previous treatments.[54,56] Using Eq. (1), assuming that $\rho_{mob}(z) = \rho_{trans}(z)$, and using, for the viscosity profile, a constant viscosity corresponding to the experimental bulk value, we obtain the velocity profile $u(z)$

shown as a blue line in Fig. 1(d), which we multiplied by a factor of 40 for better visibility. Note that while the calculation of the zeta potential via Eq. (2) needs to assume a certain dielectric response, no such assumption is needed for the conversion of the transfer-charge profile into the velocity profile via Eq. (1). It is seen that even if one assumes that the transfer charges are completely mobile, they are predicted to only produce a negligible water flow, which corresponds to a negative ζ-potential of -0.05 mV (relative to the bulk liquid) on the liquid side of the GDS, see blue line Fig. 1(d) (remember that the blue line is scaled by a factor of 40), similar to what was shown before using a more approximate calculation of the transfer-charge profile.[54] Closer to the GDS, the predicted water flow changes sign and the ζ-potential becomes positive and takes a maximal value of $+1.25$ mV, much smaller than the experimentally reported value and, in fact, of the opposite sign. We conclude that charge transfer is predicted to not produce any appreciable electrokinetic surface potential, in agreement with our explicit DFT-MD simulations in a finite electric field. It is interesting to note that the actual electrostatic potential created by the transfer-charge profile $\rho_{\text{trans}}(z)$ is larger by a factor of $\varepsilon_{\text{bulk}} = 80$ than the ζ-potential and thus rather sizable, as shown in Sec. S4 of the supplementary material. The reason for this is that the ζ-potential is by convention divided by $\varepsilon_{\text{bulk}}$, whereas the transfer-charge potential is not, since, corresponding to a polarization charge, it is itself not screened by polarization charges. This important difference must be kept in mind when comparing ζ-potentials with electrostatic surface potentials that are created by polarization or transfer charges.

The molecular transfer-charge density profile $\rho_{\text{trans}}(z)$ in Fig. 1(f) deviates from the previous results[56] for two reasons: first, in contrast to our DFT treatment, the nuclear coordinates were in previous studies sampled from FF-MD simulations, which makes a difference since the interfacial water structure deviates between DFT-MD and FF-MD simulations due to the neglect of polarization effects in FF-MD simulations: that such interfacial polarization effects are significant is demonstrated in Fig. 1(c), where we compare the water dipole moment profile from DFT-MD with the constant value assumed in our FF-MD simulations. Second, in the previous work, the charge transfer profile was determined relative to the instantaneous highly corrugated interface profile,[69,70] which makes the profile sharper. Nevertheless, the integrated charge in the negatively charged region in Fig. 1(f) amounts to a surface charge density of -0.013 e/nm^2, not so different from the value of -0.015 e/nm^2 obtained in Ref. 56. Yet, the expected electrokinetic potential due to this negative charge is about -0.05 mV and thus completely negligible compared to the experimental value of about -50 mV, as shown in Fig. 1(d). As a side comment, it is not clear at all whether the local water corrugations should actually be flattened out when analyzing the interfacial transfer-charge profile since the hydrodynamic continuous transport equations are formulated in the lab frame and not in the corrugated interfacial frame. In other words, if a tangential electrokinetic water flow would build up, it would not follow the nanoscopic water interfacial corrugations but rather follow streamlines that are rather flat in the lab frame, which means that a full three-dimensional hydrodynamic treatment should be used in the future theoretical work on electrokinetics at the air–water interface.

Although the transfer-charge profile cannot cause appreciable electrokinetic flow, even if it was mobile in an electric field, it is interesting to reveal its microscopic mechanism. According to previous arguments, the asymmetry of the hydrogen bond leads to the transfer of a minute amount of electron charge from the hydrogen-accepting to the hydrogen-donating water molecule; in the isotropic bulk, these effects cancel out, but at an interface, a net charge transfer perpendicularly to the interface can occur.[53] Indeed, the water orientational profile in terms of the cosine of the angle between the water dipole and the interface normal, $\langle \cos \theta \rangle$ in Fig. 1(e), demonstrates that the top interfacial water, where the molecular water density (green broken line) is already close to zero, points with the H atoms to the vapor (negative $\langle \cos \theta \rangle$), which gives rise to free OH bonds that dangle into the vapor phase,[71] followed by a layer further into the bulk where the H atoms point toward the liquid phase (positive $\langle \cos \theta \rangle$). We see that the ordering of DFT water (red spheres) is stronger than SPC/E FF water (black line) and extends further into the vapor. The same shift between DFT and FF water is also seen in the hydrogen–oxygen density difference profiles shown in Fig. 1(g). The interfacial water orientation, indeed, produces a local difference in the density of accepted and donated hydrogen bonds, which is quantified by the hydrogen-bond imbalance density,

$$\rho_{\Delta\text{hb}}(z) = \rho_{\text{acc}}(z) - \rho_{\text{don}}(z), \tag{4}$$

by binning all water molecules with respect to their center of mass and counting $+1$ for each accepted hydrogen bond and -1 for each donated hydrogen bond. We employ the standard geometrical definition according to which a hydrogen bond exists if oxygen atoms are less than 3.5 Å apart and the O–O–H angle is less than $30°$.[72] $\rho_{\Delta\text{hb}}(z)$ from FF-MD [black line in Fig. 1(f), left scale] compares well with previous results[54] and shows a pronounced triple-layer structure, similar to the hydrogen/oxygen density difference $\rho_{\text{H}}(z) - 2\rho_{\text{O}}(z)$ in Fig. 1(g). For the DFT data, the agreement between $\rho_{\Delta\text{hb}}(z)$ in Fig. 1(f) (red circles) and $\rho_{\text{H}}(z) - 2\rho_{\text{O}}(z)$ in Fig. 1(g) (red curve, displayed as a fit function, see Sec. S1 of supplementary material for further information) is less perfect, but we can still conclude that the interfacial hydrogen-bond imbalance profile can be qualitatively explained by the hydrogen–oxygen density difference and, thus, by the water orientation at the interface. Earlier *ab initio* studies predicted a rather small fraction of acceptor-only water molecules at the interface,[73,74] consistent with the DFT-MD hydrogen-bond imbalance in Fig. 1(f) showing a rather weak maximum in the gas phase.

We conclude that DFT and FF simulations show similar trends for the hydrogen-bond imbalance profile at the air–water interface, which, however, is not simply proportional to the transfer-charge profile: this follows from the pronounced deviation between the blue and red data points in Fig. 1(f). This means that in order to obtain accurate interfacial transfer-charge profiles, full DFT simulations have to be used. By comparing the heights of the negative humps for $\rho_{\Delta\text{hb}}(z)$ and $\rho_{\text{trans}}(z)$ in Fig. 1(f), we arrive at an estimate of the transferred charge of $0.1e$ per hydrogen bond, which is a rather high value. Nevertheless, the electrokinetic effect resulting from charge transfer, even if we assume transfer charges to be fully mobile in an externally applied electric field, is negligible, as has been shown above. This is an important lesson in connection with the discussion on the origin of the experimentally observed negative ζ-potentials of air and

oil bubbles and planar interfaces between water and hydrophobic materials.

C. Electrostatic surface potential ϕ_{ES}

We next analyze the electrostatic potential, which results from a double integration over the interfacial polarization-charge profile according to

$$\phi_{ES}(z) = -\frac{1}{\varepsilon_0} \int_{z_l}^{z} \int_{z_l}^{z'} \rho_q(z'') dz'' dz'. \quad (5)$$

For our DFT-MD results, the polarization-charge density $\rho_q(z)$ includes all nuclear and electronic charges, while for FF-MD, only the point-like partial charges of the water model contribute, in both cases, $\rho_q(z)$ results from a lateral average including the interior of all water molecules. The electrostatic potential profile $\phi_{ES}(z)$ in Fig. 2 exhibits large discrepancies between FF-MD and DFT-MD results (black and red solid lines). In rather good agreement with the literature,[7,10,11] we find the potential difference between liquid and vapor at a value of $\Delta\phi_{ES} = +4.35$ V for DFT-MD simulations and $\Delta\phi_{ES} = -0.6$ V for FF-MD simulations with the SPC/E water model. This difference is mostly due to the difference in the trace of the water quadrupolar moment, which is irrelevant for the electrostatic interaction between water molecules, and not so much due to interfacial structural differences, which are small, as has been shown in Fig. 1. The laterally averaged electrostatic potential drop at the vapor–liquid water interface has been recently measured by a combination of off-axis electron holography and liquid-phase transmission electron microscopy and found to be +4.48 V,[13] in very good agreement with our DFT-MD result. The dipolar potential contributions in Fig. 2 (broken lines) are both positive and with $\Delta\phi_{ES}^{dip} = 0.24$ V for FF and $\Delta\phi_{ES}^{dip} = 0.54$ V for DFT of similar magnitude in the liquid phase, consistent with the literature.[10,75] This reflects that the mean dipolar water orientation at the interface in Fig. 1(e) is rather similar for DFT and FF simulations. The difference between the full potential and the dipolar potential profile thus stems from quadrupolar and higher order multipole moments,
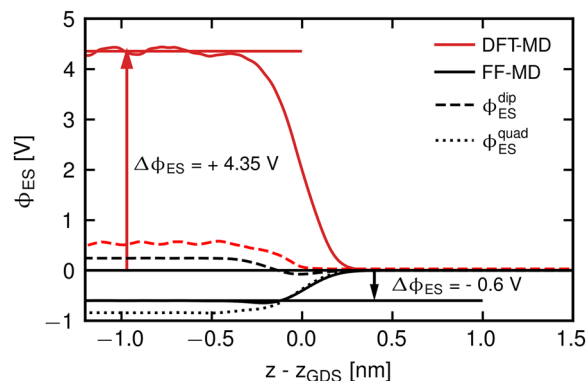

FIG. 2. Comparison of the laterally averaged electrostatic surface potential profile ϕ_{ES} from FF-MD and DFT-MD simulations (solid lines). For FF-MD, the dipolar and quadrupolar contributions ϕ_{ES}^{dip} and ϕ_{ES}^{quad} are shown as dashed and dotted black lines, for DFT-MD only the dipolar contribution is shown (red broken line).

which differ strongly between the FF and DFT models. It is important to point out that our DFT method employs pseudopotentials to represent the core electrons. This method treats the resulting core charge within the Ewald construction as a smeared-out charge density, which approximates the quadrupolar contribution of the atomic core. In Sec. S5 of the supplementary material, we compare the quadrupole moment of our DFT model with calculations that also treat the core electrons explicitly and find good agreement. This means that the way the core-electron contribution to the surface potential is accounted for in our DFT-MD simulations is accurate. The pronounced difference between the DFT and FF interface potentials in Fig. 2 can be intuitively understood by realizing that the lateral average of the electrostatic potential includes the atomic cores, which are highly positively charged in the DFT model.[11] Thus, when only averaging the DFT electrostatic potential in the space between water molecules, a surface potential much closer to FF calculations is obtained.[16]

Here, we present a complementary picture. In Fig. 3(b), we show the electrostatic potential distribution inside a water molecule
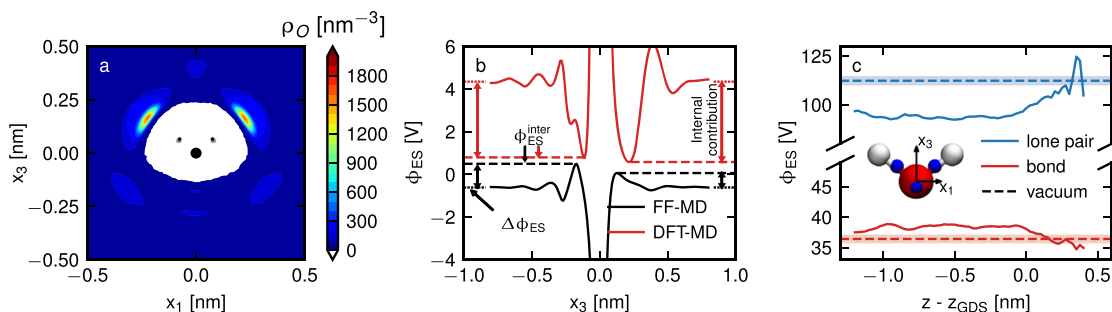

FIG. 3. Electrostatic potential inside a water molecule. (a) Oxygen nucleus number density ρ_O around a water molecule in bulk from DFT-MD simulations, averaged in a water slab of 0.2 Å thickness in the H–O–H plane. (b) Electrostatic potential ϕ_{ES} in the frame of a single water molecule in bulk along the main molecular bisector from FF-MD (black) and DFT-MD (red) simulations. The interstitial electrostatic potential ϕ_{ES}^{inter} is the potential at the boundary between water molecules, here defined by the potential extrema and denoted by broken horizontal lines. The potential far away from the central water molecule is the laterally averaged surface potential difference $\Delta\phi_{ES}$ denoted by dotted lines, the difference defines the internal contribution. (c) Electrostatic potential evaluated at the Wannier centers of the bonding (red) and lone-pair electrons (blue) as a function of the distance to the air–water interface from DFT simulations, the potentials in vacuum (located to the right) are indicated by broken horizontal lines.

in the bulk liquid phase as a function of the position x_3 along the main bisector axis, as illustrated in the inset of Fig. 3(c), from DFT-MD (red line) and FF-MD simulations (black line). This potential includes contributions not only from charges within the central water molecule but also from all neighboring ones. As expected, the potential diverges positively at the oxygen core position in DFT-MD and negatively in FF-MD, reflecting that the oxygen core charge is $+6e$ in DFT and $-0.848e$ for the SPC/E FF model.[76] At a distance to the oxygen core of $x_3 = -1.7$ and 1.3 Å for FF-MD and $x_3 = -1.1$ and 2.2 Å for DFT-MD, we find the potential magnitude to be minimal, denoted by broken horizontal lines in Fig. 3(b). These positions roughly correspond to the boundary between the central water molecule and its neighbors, which can be independently obtained from the 2D oxygen density in Fig. 3(a) around a water molecule. At these positions, the potentials are all positive and of comparable magnitude for DFT and FF, namely, 0.78 V (DFT) and 0.5 V (FF) for negative x_3 and 0.58 V (DFT) and 0.06 V (FF) for positive x_3. This reflects that at the boundary between water molecules, the difference between the DFT and FF water quadrupole moments is not important, the positive potential value reflects the positive interfacial dipolar contribution (note that the calculation is done for water molecules in the middle of a water slab with the potential in the vapor phase taken to be zero). For larger distances from the oxygen core, the potential in Fig. 3(b) averages over the interior of neighboring water molecules and thereby again picks up the water quadrupolar contribution, which is positive for DFT-MD and negative for FF-MD, and asymptotically approaches the values of $\Delta\phi_{ES} = +4.35$ V for DFT-MD and $\Delta\phi_{ES} = -0.6$ V for FF-MD (indicated by horizontal dotted lines), identical to the results in Fig. 2.

How does the electrostatic potential inside a water molecule depend on the separation from the air–water interface? For this, one has to choose a water-internal position. In Fig. 3(c), we show the electrostatic potential at the position of the charge centers of maximally localized Wannier functions corresponding to an effective position of the bonding electrons (red line) and the lone-pair electrons (blue line) as a function of the position of the Wannier centers relative to the GDS of the vapor–water interface; here, we only show DFT results. As one moves into liquid bulk water (located to the left), the electrostatic potential shifts away from the vacuum values (denoted by broken horizontal lines) and reaches a potential difference in bulk of $\phi_{ES}^{bulk} - \phi_{ES}^{vac} = 1.94$ V for bonding electrons and $\phi_{ES}^{bulk} - \phi_{ES}^{vac} = -18.2$ V for lone-pair electrons. Note that these potentials are also influenced by the positions of the Wannier centers, which shift slightly as the water molecule approaches the interface. These results demonstrate how important the position relative to the water molecule coordinate frame is where the electrostatic potential is evaluated. Such surface potentials are relevant for surface-sensitive experimental techniques that probe the electrostatic potential inside the water molecules, such as photoelectron spectroscopy[31] or SHG or SFG.[29,32–34]

D. Electrochemical surface potential ϕ_{EC}

None of the electrostatic potentials discussed so far reflects the electrostatic potential an atom or ion experiences as it approaches the air–water interface. This is so because when an atom or ion is inserted into water, the water structure is perturbed and an

oriented hydration layer forms around it, which produces an additional electrostatic potential contribution, while the potential contribution due to the trace of the quadrupolar tensor of neighboring water molecules does not contribute.[16,18,77–79] Here, we define the electrochemical potential as the part of the electrostatic solvation work that is linear in the ion charge, which corresponds to the electrostatic potential within a neutral atom with respect to the vapor phase (note that the quadratic contribution to the electrostatic solvation free energy is given by the Born dielectric energy while also higher-order contributions exist and can be quite sizable[20,21]). As illustrated in Fig. 4(a), we introduce a single argon into the water-slab system at different separations from the interface and calculate the electrostatic potential in the center of the argon atom excluding contributions from the atom itself.

In Fig. 4(b), we show the electrostatic potential from FF-MD on a line that passes through the center of an argon atom that is held at a fixed separation of 0.47 nm from the air–water interface. As the air–water interface is crossed, the potential drops to $\Delta\phi_{ES} = -0.6$ V, as discussed before. The hydration layer around the argon atom largely compensates for this potential and gives rise to a remaining electrochemical potential in the argon center of only $\phi_{EC} = -0.2$ V. The compensation is thus not complete, since the hydration layers at the planar air–water interface and around the argon atom exhibit different degrees of water orientation. In Figs. 4(e) and 4(f), we show the so-called cavity potential profile ϕ_{cav} around the different noble gas atoms helium, neon, argon, and krypton in bulk water as a function of the radial distance from the atom center; here, the potential is calculated with respect to the atom center. One can interpret the calculation for He as an approximation for the case of Li$^+$, Ne as an approximation of F$^-$ and Na$^+$, Ar as an approximation of Cl$^-$ and K$^+$, and Kr as an approximation of Br$^-$ and Rb$^+$. For the DFT-MD simulations, we radially average the Hartree electrostatic potential output on a grid, and for FF-MD simulations, we solve the Poisson equation using the radially averaged water partial-charge distribution. The FF-MD profiles saturate for $r > 1.2$ nm and thereby yield the cavity potential difference $\Delta\phi_{cav}$. The DFT-MD do not saturate at half of the used box length $L = 1.98$ nm, in order to determine $\Delta\phi_{cav}$, we average the electrostatic potential for $r > L/2$, which results in the horizontal dashed lines in Fig. 4(e). The electrochemical potential $\Delta\phi_{EC}$ follows by subtracting the cavity potential from the air–water surface potential according to

$$\Delta\phi_{EC} = \Delta\phi_{ES} - \Delta\phi_{cav}, \qquad (6)$$

and is equivalent to the so-called net potential ϕ_{np} in Beck[16] and the cavity potential ϕ_{HW} in Remsing et al.[10] First of all, the values of $\Delta\phi_{EC}$ shown in Fig. 4(c) for the different atoms are rather similar for FF and DFT simulations, demonstrating that the huge differences of $\Delta\phi_{ES}$ between DFT and FF, indeed, largely cancel out. Second, $\Delta\phi_{EC}$ shows a clear size dependence, which differs quite significantly between FF and DFT. For FF-MD simulations, the electrochemical potential decreases with increasing atom size, consistent with trends found previously.[10,18,80] In contrast, the DFT-MD results exhibit a sign change when going from the smallest He atom to the larger atoms, which points to an interesting size anomaly. Previous studies using hard-sphere exclusion potentials found negative electrochemical potentials using FF simulation methods for different cavity sizes, in rough agreement with our finding, and different results for DFT
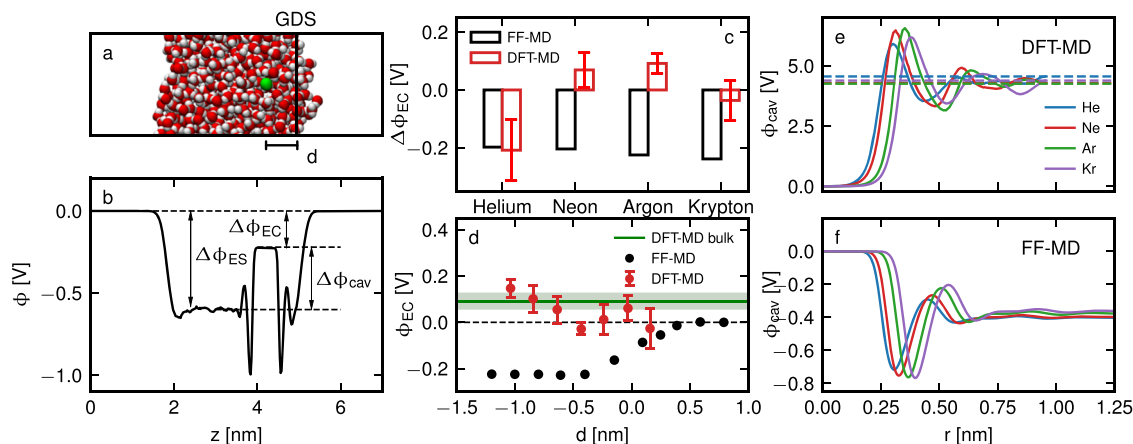
FIG. 4. (a) Snapshot from an FF-MD simulation of a single argon atom in a water slab. (b) Electrostatic potential profile ϕ_{ES} from FF-MD of the system shown in (a) on a line through the argon center, the surface potential $\Delta\phi_{ES}$, the electrochemical potential $\Delta\phi_{EC}$, and the cavity potential $\Delta\phi_{cav}$ is indicated. (c) Electrochemical potential of different noble gas atoms from DFT and FF-MD simulations. (d) Electrochemical potential profile of an argon atom as a function of the distance from the air–water interface from DFT and FF-MD simulations. (e) and (f) Cavity potential profiles from DFT-MD and FF-MD simulations in bulk water, horizontal dashed lines indicate the averaged DFT bulk potential.

models that depend on details of the density functional used in the simulations.[10] Thus, we conclude that details of the employed simulation method and the interaction model between the cavity and the surrounding water are highly relevant, which reflects that the electrochemical potential results from subtracting two rather large potential contributions from each other.

We also calculate the electrochemical potential profile by placing an argon atom at different positions inside the air–water slab system. The potential profiles $\phi_{EC}(z)$ from DFT and FF simulations in Fig. 4(d) show a smooth crossover from zero (in the vapor phase) to the value $\Delta\phi_{EC}$ in the bulk phase, which differs between FF and DFT. The width of this crossover is roughly two times the width of the electrostatic potential profile $\phi_{ES}(z)$. From our FF-MD data, we find a width of 0.29 nm for $\phi_{ES}(z)$ in Fig. 2 and 0.63 nm for $\phi_{EC}(z)$ in Fig. 4(d) (see Sec. S6 of the supplementary material for details of the calculation). Thus, the electrochemical potential width is substantial and of the order of the Debye screening length for 150 mM salt, which is relevant for the accurate prediction and interpretation of ionic density profiles at aqueous interfaces.

III. CONCLUSION

We show that at least four different surface potentials can be defined, which are relevant to describe distinct experimental setups. These are the electrokinetic potential ϕ_{EK}, the electrostatic potential ϕ_{ES}, which comes in two different versions, namely, the laterally averaged electrostatic potential and the electrostatic potential at fixed positions inside a water molecule, and the electrochemical potential ϕ_{EC}, which, here, is defined as the potential inside a noble gas atom (even more surface potentials exist and are relevant for diverse scenarios, for example, the surface potential from water transfer charges that is shown in the supplementary material). We calculate each of them on the same level of theory from DFT-MD as well as from FF-MD simulations as a function of the separation from the air–water interface.

In particular, we derive the electrokinetic potential from *ab initio* simulations of an air–water interface by explicitly applying a tangential electric field and show that although significant charge transfer takes place, the ζ-potential of the neat vapor–water interface is zero within the error bounds, suggesting that intermolecular charge transfer does not induce electrokinetic mobility on an experimentally relevant scale of magnitude. The same conclusion actually follows from the Helmholtz–Smoluchowski equation applied to the transfer-charge profile extracted from DFT-MD simulations.

The laterally averaged electrostatic potential from our DFT-MD simulations is +4.35 V, close to earlier theoretical work[7,10,81] and in good agreement with recent experimental electron holography measurements.[13] The analysis of the electrostatic potential within a water molecule reconfirms that the main contributions to the laterally averaged DFT surface potential come from the water quadrupole moment.

When we evaluate the electrostatic potential acting on the lone-pair and the binding electrons within water molecules, we find significant changes as a function of the separation from the interface. This presumably is relevant for surface sensitive techniques that measure electrostatic potentials inside water molecules like photo-electron spectroscopy and non-linear spectroscopy.

We also determine the surface potential within neutral noble gas atoms of different sizes and for different separations from the air–water interface, which reflects the electrochemical potential acting on different ions. In DFT, we find a strong size dependence and, in particular, different signs of the electrochemical potential for helium with respect to the larger noble gas atoms.

The picture that emerges from our comparative simulation studies is that different experiments probe vastly different surface potentials, which, however, can be all derived from simulations and only together allow to draw a coherent and complete picture of the electrostatic properties of the air–water interface. It transpires that FF simulation models work reasonably well for ion distributions, i.e.,

when the internal water charge distribution is irrelevant, while DFT simulations are needed when the internal water charge distribution is relevant, i.e., for describing electron holography experiments or photo-electron and non-linear optical spectroscopy experiments at interfaces.

IV. METHODS

A. DFT and FF MD simulations

All FF-MD simulations are conducted in Gromacs 2020 using the SPC/E water model with Particle Mesh Ewald (PME) electrostatics and a 0.9 nm van-der-Waals cut-off. The van-der-Waals potential is shifted to zero at the cutoff distance. We employ a time step of 2 fs. DFT-MD simulations are carried out using the CP2K 6.1 version[82] by the Born–Oppenheimer approximation. We employ the BLYP functional with Grimme D3 dispersion correction,[83] Goedecker-Teter-Hutter (GTH) pseudopotentials, and combine it with the DZVP-SR-MOLOPT basis set using a plane wave cutoff of 400 Ry. All DFT-MD simulations use a time step of 0.5 fs. In general, the density of *ab initio* water depends quite strongly not only on the exchange correlation functional but also on the employed dispersion correction as well as the basis set. DFT simulations employing the BLYP exchange correlation functional underestimate the density of liquid water quite substantially. Adding the Grimme dispersion correction usually overcompensates and leads to an overestimated density.[84–87] The DZVP-SR-MOLOPT basis set we employ in this work overestimates the density compared to previous studies using a TZV2P basis set, which predicts values very close to the experimental ones, but conserves structure and dynamics well.[87,88] In particular, for the calculation of ζ-potentials, long trajectories are needed, so we opt for the smaller basis set due to the gain in computational performance.

B. Vapor–water slab simulations

We conduct simulations of 352 water molecules in a periodic box of $2 \times 2 \times 6$ nm^3 resulting in a stable slab of roughly 3 nm thickness. After an FF simulation with 1 ns equilibration time, we perform subsequent production runs of 20 ns. Using an FF-MD equilibrated configuration as input, we conduct 110 ps of DFT simulation of which we disregard the first 10 ps for further equilibration purposes. We calculate the molecular dipoles shown in Fig. 1(c) from the charge centers of maximally localized Wannier functions. From the density profiles depicted in Fig. 1(b), we calculate the position of the GDS according to

$$z_{GDS} = \int_{z_l}^{z_v} \frac{\rho_v - \rho(z)}{\rho_v - \rho_l} dz. \tag{7}$$

The electrostatic potential is evaluated from the volumetric data that CP2K writes out. Directly averaging the potential gives identical results compared to writing out the full charge density and integrating it according to the Poisson equation. We fit the electrostatic potential profiles shown in Fig. 2 with tanh profiles. These fits result in the vapor-bulk potential differences of 4.35 and −0.6 V for DFT and FF simulations, respectively. All molecular properties, such as the molecular dipole moment in Fig. 1(c), the molecular velocity profile in Fig. 1(d), the orientational profile in Fig. 1(e), the hydrogen

bond imbalance in Fig. 1(f), and the quadrupolar and dipolar contributions shown in Fig. 2 are binned with respect to the molecular center of mass positions.

C. Electrokinetic simulations

Starting from a fully DFT-equilibrated system configuration (see Sec. S1 of the supplementary material), we conduct a 120 ps simulation with an external E-field of $E_\parallel = 0.5 \cdot 10^{-4} \frac{E_h}{ea_0} \approx 257 \text{mV/nm}$. Electric fields are applied according to the method introduced by Umari and Pasquarello.[58] We disregard the first 25 ps of the simulation for equilibration purposes. This corresponds to a full relaxation of the in-field component of the total system polarization (see Sec. S1 of the supplementary material).

D. Electrochemical potentials

We place a single argon atom at different distances from the interface into a vapor–water slab by replacing one of the water molecules of the slab shown in Fig. 1(a). We conduct DFT simulations of these systems for at least 30 ps for each configuration and disregard the first 5 ps in the evaluation. We evaluate the potential difference between the inner of the cavity and the vapor phase every 50 fs. For FF results, we use a water slab of 648 water molecules. Since the individual water molecules of the gas phase that cross over the periodic boundary conditions lead to a minor movement of the center of mass of the slab, we place a solid wall at $z = 0$ nm to repel water molecules. We collect 200 ns of statistics for every distance and evaluate the electrochemical potential with an Ewald summation of all charges in post processing.

E. Vacuum properties of water molecules

The water dipole moment and the interior water potential in vacuum are calculated from NVT single water DFT-MD simulations in a $2 \times 2 \times 2$ nm^3 box, sampling over 10 ps statistics.

F. Error evaluation

Error bars are calculated by using the reblocking technique introduced in Ref. 89. For z-dependent data, time series are considered for every z-bin and reblocked individually. In the case of the electrochemical potentials shown in Fig. 4(c), we calculate the error bars for the water cavity potential $\Delta\phi_{cav}$ and for the air–water surface potential $\Delta\phi_{ES}$ and add up the resulting variances.

SUPPLEMENTARY MATERIAL

See the supplementary material for details of analysis procedures, additional data, and discussion.

AUTHOR DECLARATIONS

Conflict of Interest

The authors have no conflicts to disclose.

Author Contributions

Maximilian R. Becker: Conceptualization (equal); Data curation (equal); Formal analysis (equal); Investigation (equal); Methodology (equal); Software (equal); Validation (equal); Visualization (equal); Writing – original draft (equal); Writing – review & editing (equal). **Philip Loche**: Conceptualization (supporting); Methodology (supporting); Software (supporting). **Roland R. Netz**: Conceptualization (equal); Funding acquisition (equal); Project administration (equal); Supervision (equal); Writing – original draft (equal); Writing – review & editing (equal).

DATA AVAILABILITY

The data that support the findings of this study are available from the corresponding author upon reasonable request.

REFERENCES

[1] G. Gonella, E. H. G. Backus, Y. Nagata, D. J. Bonthuis, P. Loche, A. Schlaich, R. R. Netz, A. Kühnle, I. T. McCrum, M. T. M. Koper *et al.*, "Water at charged interfaces," Nat. Rev. Chem. **5**, 466–485 (2021).

[2] D. Horinek, A. Herz, L. Vrbka, F. Sedlmeier, S. I. Mamatkulov, and R. R. Netz, "Specific ion adsorption at the air/water interface: The role of hydrophobic solvation," Chem. Phys. Lett. **479**, 173–183 (2009).

[3] D. J. Tobias, A. C. Stern, M. D. Baer, Y. Levin, and C. J. Mundy, "Simulation and theory of ions at atmospherically relevant aqueous liquid-air interfaces," Annu. Rev. Phys. Chem. **64**, 339–359 (2013); arXiv:1306.6858.

[4] S. I. Mamatkulov, C. Allolio, R. R. Netz, and D. J. Bonthuis, "Orientation-induced adsorption of hydrated protons at the air–water interface," Angew. Chem., Int. Ed. **56**, 15846–15851 (2017).

[5] M. A. Wilson, A. Pohorille, and L. R. Pratt, "Surface potential of the water liquid–vapor interface," J. Chem. Phys. **88**, 3281–3285 (1988).

[6] M. A. Wilson, A. Pohorille, and L. R. Pratt, "Comment on 'Study on the liquid–vapor interface of water. I. Simulation results of thermodynamic properties and orientational structure,'" J. Chem. Phys. **90**, 5211 (1989).

[7] K. Leung, "Surface potential at the air–water interface computed using density functional theory," J. Phys. Chem. Lett. **1**, 496–499 (2010); arXiv:1009.4162.

[8] D. J. Bonthuis, S. Gekle, and R. R. Netz, "Profile of the static permittivity tensor of water at interfaces: Consequences for capacitance, hydration interaction and ion adsorption," Langmuir **28**, 7679–7694 (2012).

[9] S. M. Kathmann, I.-F. W. Kuo, and C. J. Mundy, "Electronic effects on the surface potential at the vapor-liquid interface of water," J. Am. Chem. Soc. **131**, 17522 (2009).

[10] R. C. Remsing, M. D. Baer, G. K. Schenter, C. J. Mundy, and J. D. Weeks, "The role of broken symmetry in solvation of a spherical cavity in classical and quantum water models," J. Phys. Chem. Lett. **5**, 2767–2774 (2014).

[11] S. M. Kathmann, I.-F. W. Kuo, C. J. Mundy, and G. K. Schenter, "Understanding the surface potential of water," J. Phys. Chem. B **115**, 4369–4377 (2011).

[12] A. Harscher and H. Lichte, "Inelastic mean free path and mean inner potential of carbon foil and vitrified ice measured with electron holography," in *ICEM14, Cancun, Mexico, 31 August–4 September,* edited by H. A. Calderon-Benavides and M.-J. Yacaman (Institute of Physics Publishing, Philadelphia, PA, 1998), p. 553–554.

[13] M. N. Yesibolati, S. Laganà, H. Sun, M. Beleggia, S. M. Kathmann, T. Kasama, and K. Mølhave, "Mean inner potential of liquid water," Phys. Rev. Lett. **124**, 065502 (2020).

[14] P. Hunenberger and M. Reif, *Single-Ion Solvation*, Theoretical and Computational Chemistry Series (The Royal Society of Chemistry, 2011), pp. P001–P664.

[15] R. C. Remsing and J. D. Weeks, "The influence of distant boundaries on the solvation of charged particles," J. Stat. Phys. **175**, 743–763 (2019); arXiv:1902.00779.

[16] T. L. Beck, "The influence of water interfacial potentials on ion hydration in bulk water and near interfaces," Chem. Phys. Lett. **561–562**, 1–13 (2013).

[17] T. T. Duignan, M. D. Baer, G. K. Schenter, and C. J. Mundy, "Electrostatic solvation free energies of charged hard spheres using molecular dynamics with density functional theory interactions," J. Chem. Phys. **147**, 161716 (2017); arXiv:1702.05203.

[18] T. T. Duignan, M. D. Baer, G. K. Schenter, and C. J. Mundy, "Real single ion solvation free energies with quantum mechanical simulation," Chem. Sci. **8**, 6131–6140 (2017); arXiv:1703.03865.

[19] P. Loche, C. Ayaz, A. Schlaich, D. J. Bonthuis, and R. R. Netz, "Breakdown of linear dielectric theory for the interaction between hydrated ions and graphene," J. Phys. Chem. Lett. **9**, 6463–6468 (2018).

[20] P. Loche, L. Scalfi, M. Ali Amu, O. Schullian, D. J. Bonthuis, B. Rotenberg, and R. R. Netz, "Effects of surface rigidity and metallicity on dielectric properties and ion interactions at aqueous hydrophobic interfaces," J. Chem. Phys. **157**, 094707 (2022).

[21] P. Loche, D. J. Bonthuis, and R. R. Netz, "Molecular dynamics simulations of the evaporation of hydrated ions from aqueous solution," Commun. Chem. **5**, 55 (2022).

[22] A. Kubincová, P. H. Hünenberger, and M. Krishnan, "Interfacial solvation can explain attraction between like-charged objects in aqueous solution," J. Chem. Phys. **152**, 104713 (2020); arXiv:1911.04442.

[23] A. Behjatian, R. Walker-Gibbons, A. A. Schekochihin, and M. Krishnan, "Nonmonotonic pair potentials in the interaction of like-charged objects in solution," Langmuir **38**, 786–800 (2022).

[24] R. R. Netz and H. Orland, "Beyond Poisson-Boltzmann: Fluctuation effects and correlation functions," Eur. Phys. J. E **1**, 203–214 (2000).

[25] A. G. Moreira and R. R. Netz, "Binding of similarly charged plates with counterions only," Phys. Rev. Lett. **87**, 078301 (2001).

[26] R. R. Netz, "Electrostatics of counter-ions at and between planar charged walls: From Poisson-Boltzmann to the strong-coupling theory," Eur. Phys. J. E **5**, 557–574 (2001).

[27] N. L. Jarvis and M. A. Scheiman, "Surface potentials of aqueous electrolyte solutions," J. Phys. Chem. **72**, 74–78 (1968).

[28] T. Adel, J. Velez-Alvarez, A. C. Co, and H. C. Allen, "Circuit analysis of ionizing surface potential measurements of electrolyte solutions," J. Electrochem. Soc. **168**, 016507 (2021).

[29] L. B. Dreier, C. Bernhard, G. Gonella, E. H. G. Backus, and M. Bonn, "Surface potential of a planar charged lipid-water interface. What do vibrating plate methods, second harmonic and sum frequency measure?," J. Phys. Chem. Lett. **9**, 5685–5691 (2018).

[30] M. A. Brown, Z. Abbas, A. Kleibert, R. G. Green, A. Goel, S. May, and T. M. Squires, "Determination of surface potential and electrical double-layer structure at the aqueous electrolyte-nanoparticle interface," Phys. Rev. X **6**, 011007 (2016).

[31] S. Thürmer, S. Malerz, F. Trinter, U. Hergenhahn, C. Lee, D. M. Neumark, G. Meijer, B. Winter, and I. Wilkinson, "Accurate vertical ionization energy and work function determinations of liquid water and aqueous solutions," Chem. Sci. **12**, 10558–10582 (2021).

[32] A. Marchioro, M. Bischoff, C. Lütgebaucks, D. Biriukov, M. Předota, and S. Roke, "Surface characterization of colloidal silica nanoparticles by second harmonic scattering: Quantifying the surface potential and interfacial water order," J. Phys. Chem. C **123**, 20393–20404 (2019).

[33] E. Ma and F. M. Geiger, "Divalent ion specific outcomes on Stern layer structure and total surface potential at the silica:water interface," J. Phys. Chem. A **125**, 10079–10088 (2021).

[34] E. Ma, P. E. Ohno, J. Kim, Y. Liu, E. H. Lozier, T. F. Miller, H.-F. Wang, and F. M. Geiger, "A new imaginary term in the second-order nonlinear susceptibility from charged interfaces," J. Phys. Chem. Lett. **12**, 5649–5659 (2021).

[35] S. Usui and H. Sasaki, "Zeta potential measurements of bubbles in aqueous surfactant solutions," J. Colloid Interface Sci. **65**, 36–45 (1978).

[36]S. Usui, H. Sasaki, and H. Matsukawa, "The dependence of zeta potential on bubble size as determined by the Dorn effect," J. Colloid Interface Sci. **81**, 80–84 (1981).

[37]M. Takahashi, "ζ potential of microbubbles in aqueous solutions: Electrical properties of the gas–water interface," J. Phys. Chem. B **109**, 21858–21864 (2005).

[38]C. Oliveira and J. Rubio, "Zeta potential of single and polymer-coated microbubbles using an adapted microelectrophoresis technique," Int. J. Miner. Process. **98**, 118–123 (2011).

[39]L. M. Pegram and M. T. Record, "Partitioning of atmospherically relevant ions between bulk water and the water/vapor interface," Proc. Natl. Acad. Sci. U. S. A. **103**, 14278–14281 (2006).

[40]Y. Uematsu, D. J. Bonthuis, and R. R. Netz, "Impurity effects at hydrophobic surfaces," Curr. Opin. Electrochem. **13**, 166–173 (2019).

[41]R. J. Saykally, "Evidence for an enhanced proton concentration at the liquid water surface from SHG spectroscopy," in *Frontiers in Optics 2007/Laser Science XXIII/Organic Materials and Devices for Displays and Energy Conversion*, OSA Technical Digest (CD) (Optica Publishing Group, 2007), paper LTuC1.

[42]V. Buch, A. Milet, R. Vácha, P. Jungwirth, and J. P. Devlin, "Water surface is acidic," Proc. Natl. Acad. Sci. U. S. A. **104**, 7342–7347 (2007).

[43]X. Yan, M. Delgado, J. Aubry, O. Gribelin, A. Stocco, F. Boisson-Da Cruz, J. Bernard, and F. Ganachaud, "Central role of bicarbonate anions in charging water/hydrophobic interfaces," J. Phys. Chem. Lett. **9**, 96–103 (2018).

[44]Y. Uematsu, D. J. Bonthuis, and R. R. Netz, "Charged surface-active impurities at nanomolar concentration induce Jones–Ray effect," J. Phys. Chem. Lett. **9**, 189–193 (2018).

[45]L. Joly, F. Detcheverry, and A. L. Biance, "Anomalous ζ potential in foam films," Phys. Rev. Lett. **113**, 088301 (2014).

[46]Y. Uematsu, D. J. Bonthuis, and R. R. Netz, "Nanomolar surface-active charged impurities account for the zeta potential of hydrophobic surfaces," Langmuir **36**, 3645–3658 (2020).

[47]S. Pullanchery, S. Kulik, H. I. Okur, H. B. De Aguiar, and S. Roke, "On the stability and necessary electrophoretic mobility of bare oil nanodroplets in water," J. Chem. Phys. **152**, 241104 (2020).

[48]V. Knecht, H. J. Risselada, A. E. Mark, and S. J. Marrink, "Electrophoretic mobility does not always reflect the charge on an oil droplet," J. Colloid Interface Sci. **318**, 477–486 (2008).

[49]S. Joseph and N. R. Aluru, "Pumping of confined water in carbon nanotubes by rotation-translation coupling," Phys. Rev. Lett. **101**, 064502 (2008).

[50]D. J. Bonthuis, D. Horinek, L. Bocquet, and R. R. Netz, "Electrohydraulic power conversion in planar nanochannels," Phys. Rev. Lett. **103**, 144503 (2009).

[51]D. J. Bonthuis, D. Horinek, L. Bocquet, and R. R. Netz, "Electrokinetics at aqueous interfaces without mobile charges," Langmuir **26**, 12614–12625 (2010).

[52]D. J. Bonthuis, K. Falk, C. N. Kaplan, D. Horinek, A. N. Berker, L. Bocquet, and R. R. Netz, "Comment on 'Pumping of confined water in carbon nanotubes by rotation-translation coupling,'" Phys. Rev. Lett. **105**, 209401 (2010).

[53]R. Vácha, S. W. Rick, P. Jungwirth, A. G. F. de Beer, H. B. de Aguiar, J.-S. Samson, and S. Roke, "The orientation and charge of water at the hydrophobic oil droplet–water interface," J. Am. Chem. Soc. **133**, 10204–10210 (2011).

[54]R. Vácha, O. Marsalek, A. P. Willard, D. J. Bonthuis, R. R. Netz, and P. Jungwirth, "Charge transfer between water molecules as the possible origin of the observed charging at the surface of pure water," J. Phys. Chem. Lett. **3**, 107–111 (2012).

[55]C. D. Wick, A. J. Lee, and S. W. Rick, "How intermolecular charge transfer influences the air-water interface," J. Chem. Phys. **137**, 154701 (2012).

[56]E. Poli, K. H. Jong, and A. Hassanali, "Charge transfer as a ubiquitous mechanism in determining the negative charge at hydrophobic interfaces," Nat. Commun. **11**, 901 (2020).

[57]A. Wolde-Kidan and R. R. Netz, "Interplay of interfacial viscosity, specific-ion, and impurity adsorption determines zeta potentials of phospholipid membranes," Langmuir **37**, 8463–8473 (2021).

[58]P. Umari and A. Pasquarello, "*Ab initio* molecular dynamics in a finite homogeneous electric field," Phys. Rev. Lett. **89**, 157602 (2002).

[59]A. M. Saitta, F. Saija, and P. V. Giaquinta, "*Ab initio* molecular dynamics study of dissociation of water under an electric field," Phys. Rev. Lett. **108**, 207801 (2012).

[60]A. Calzolari and M. B. Nardelli, "Dielectric properties and Raman spectra of ZnO from a first principles finite-differences/finite-fields approach," Sci. Rep. **3**, 2999 (2013).

[61]D. J. Bonthuis and R. R. Netz, "Unraveling the combined effects of dielectric and viscosity profiles on surface capacitance, electro-osmotic mobility, and electric surface conductivity," Langmuir **28**, 16049–16059 (2012).

[62]C. G. Malmberg and A. A. Maryott, "Dielectric constant of water from $0°$ to $100°C$," J. Res. Natl. Bur. Stand. **56**(1), 2641 (1956).

[63]K. E. Bett and J. B. Cappi, "Effect of pressure on the viscosity of water," Nature **207**, 620–621 (1965).

[64]J. C. Schulz, A. Schlaich, M. Heyden, R. R. Netz, and J. Kappler, "Molecular interpretation of the non-Newtonian viscoelastic behavior of liquid water at high frequencies," Phys. Rev. Fluids **5**, 103301 (2020); arXiv:2003.08309.

[65]A. P. Markesteijn, R. Hartkamp, S. Luding, and J. Westerweel, "A comparison of the value of viscosity for several water models using Poiseuille flow in a nano-channel," J. Chem. Phys. **136**, 134104 (2012).

[66]Y. S. Badyal, M.-L. Saboungi, D. L. Price, S. D. Shastri, D. R. Haeffner, and A. K. Soper, "Electron distribution in water," J. Chem. Phys. **112**, 9206–9208 (2000).

[67]S. A. Clough, Y. Beers, G. P. Klein, and L. S. Rothman, "Dipole moment of water from Stark measurements of H_2O, HDO, and D_2O," J. Chem. Phys. **59**, 2254–2259 (1973).

[68]T. A. Manz and N. G. Limas, "Introducing DDEC6 atomic population analysis: Part 1. Charge partitioning theory and methodology," RSC Adv. **6**, 47771–47801 (2016).

[69]F. Sedlmeier, D. Horinek, and R. R. Netz, "Nanoroughness, intrinsic density profile, and rigidity of the air-water interface," Phys. Rev. Lett. **103**, 136102 (2009).

[70]A. P. Willard and D. Chandler, "Instantaneous liquid interfaces," J. Phys. Chem. B **114**, 1954–1958 (2010).

[71]S. Sun, F. Tang, S. Imoto, D. R. Moberg, T. Ohto, F. Paesani, M. Bonn, E. H. G. Backus, and Y. Nagata, "Orientational distribution of free O-H groups of interfacial water is exponential," Phys. Rev. Lett. **121**, 246101 (2018).

[72]A. Luzar and D. Chandler, "Hydrogen-bond kinetics in liquid water," Nature **379**, 55–57 (1996).

[73]I.-F. W. Kuo and C. J. Mundy, "An ab initio molecular dynamics study of the aqueous liquid-vapor interface," Science **303**, 658–660 (2004).

[74]T. D. Kühne, T. A. Pascal, E. Kaxiras, and Y. Jung, "New insights into the structure of the vapor/water interface from large-scale first-principles simulations," J. Phys. Chem. Lett. **2**, 105–113 (2011).

[75]M. Sulpizi, M. Salanne, M. Sprik, and M.-P. Gaigeot, "Vibrational sum frequency generation spectroscopy of the water liquid–vapor interface from density functional theory-based molecular dynamics simulations," J. Phys. Chem. Lett. **4**, 83–87 (2013).

[76]H. J. C. Berendsen, J. R. Grigera, and T. P. Straatsma, "The missing term in effective pair potentials," J. Phys. Chem. **91**, 6269–6271 (1987).

[77]M. D. Baer, A. C. Stern, Y. Levin, D. J. Tobias, and C. J. Mundy, "Electrochemical surface potential due to classical point charge models drives anion adsorption to the air–water interface," J. Phys. Chem. Lett. **3**, 1565–1570 (2012).

[78]L. Horváth, T. Beu, M. Manghi, and J. Palmeri, "The vapor-liquid interface potential of (multi)polar fluids and its influence on ion solvation," J. Chem. Phys. **138**, 154702 (2013).

[79]T. S. Hofer and P. H. Hünenberger, "Absolute proton hydration free energy, surface potential of water, and redox potential of the hydrogen electrode from first principles: QM/MM MD free-energy simulations of sodium and potassium hydration," J. Chem. Phys. **148**, 222814 (2018).

[80]S. J. Cox, D. G. Thorpe, P. R. Shaffer, and P. L. Geissler, "Assessing long-range contributions to the charge asymmetry of ion adsorption at the air–water interface," Chem. Sci. **11**, 11791–11800 (2020).

[81]S. M. Kathmann, I.-F. W. Kuo, and C. J. Mundy, "Electronic effects on the surface potential at the vapor-liquid interface of water," J. Am. Chem. Soc. **130**, 16556–16561 (2008).

[82] J. Hutter, M. Iannuzzi, F. Schiffmann, and J. Vandevondele, "CP2K: Atomistic simulations of condensed matter systems," Wiley Interdiscip. Rev.: Comput. Mol. Sci. **4**, 15–25 (2014).

[83] S. Grimme, J. Antony, S. Ehrlich, and H. Krieg, "A consistent and accurate *ab initio* parametrization of density functional dispersion correction (DFT-D) for the 94 elements H-Pu," J. Chem. Phys. **132**, 154104 (2010).

[84] Z. Ma, Y. Zhang, and M. E. Tuckerman, "*Ab initio* molecular dynamics study of water at constant pressure using converged basis sets and empirical dispersion corrections," J. Chem. Phys. **137**, 044506 (2012).

[85] M. Del Ben, M. Schönherr, J. Hutter, and J. Vandevondele, "Bulk liquid water at ambient temperature and pressure from MP2 theory," J. Phys. Chem. Lett. **4**, 3753–3759 (2013).

[86] M. Del Ben, J. Hutter, and J. VandeVondele, "Probing the structural and dynamical properties of liquid water with models including non-local electron correlation," J. Chem. Phys. **143**, 054506 (2015).

[87] M. J. Gillan, D. Alfè, and A. Michaelides, "Perspective: How good is DFT for water?," J. Chem. Phys. **144**, 130901 (2016); arXiv:1603.01990.

[88] J. Schmidt, J. Vandevondele, I.-F. W. Kuo, D. Sebastiani, J. I. Siepmann, J. Hutter, and C. J. Mundy, "Isobaric-isothermal molecular dynamics simulations utilizing density functional theory: An assessment of the structure and density of water at near-ambient conditions," J. Phys. Chem. B **113**, 11959–11964 (2009).

[89] H. Flyvbjerg and H. G. Petersen, "Error estimates on averages of correlated data," J. Chem. Phys. **91**, 461–466 (1989).